

This is the accepted manuscript made available via CHORUS. The article has been published as:

Quasiparticle self-consistent

G band structures and high-pressure phase transitions of

LiGaO_2 and NaGaO_2

Santosh Kumar Radha, Amol Ratnaparkhe, and Walter R. L. Lambrecht

Phys. Rev. B **103**, 045201 — Published 6 January 2021

DOI: [10.1103/PhysRevB.103.045201](https://doi.org/10.1103/PhysRevB.103.045201)

Quasiparticle self-consistent GW band structures and high-pressure phase transitions of LiGaO_2 and NaGaO_2

Santosh Kumar Radha, Amol Ratnaparkhe and Walter R. L. Lambrecht
*Department of Physics, Case Western Reserve University,
10900 Euclid Avenue, Cleveland, Ohio 44106-7079, USA*

Quasi-particle self-consistent GW calculations are presented for the band structures of LiGaO_2 and NaGaO_2 in the orthorhombic $Pna2_1$ tetrahedrally coordinated crystal structures, which are closely related to the wurtzite structure of ZnO . Symmetry labeling of the bands near the gap is carried out and effective mass tensors are extracted for the conduction band minimum and crystal field split valence band maxima at Γ . The gap is found to be direct at Γ and is 5.81 eV in LiGaO_2 and 5.46 eV in NaGaO_2 . Electron-phonon coupling zero-point normalization is estimated to lower these gaps by about 0.2 ± 0.1 eV. Optical response functions are calculated within the independent particle long wavelength limit and show the expected anisotropy of the absorption onsets due to the crystal field splitting of the VBM. The results show that both materials are promising candidates as ultrawide gap semiconductors with wurtzite based tetrahedrally bonded crystal structures. Direct transitions from the lowest conduction band to higher bands, relevant to n-type doped material and transparent conduction applications are found to start only above 3.9 eV and are allowed for only one polarization, and several higher band transitions are forbidden by symmetry. Alternative crystal structures, such as $R\bar{3}m$ and a rocksalt type phase with tetragonally distorted $P4/mmm$ spacegroup, both with octahedral coordination of the cations are also investigated. They are found to have higher energy but about 20 % smaller volume per formula unit. The transition pressures to these phases are determined and for LiGaO_2 found to be in good agreement with experimental studies. The $R\bar{3}m$ phase also has a comparably high but slightly indirect band gap while the rocksalt type phase is found to have a considerably smaller gap of about 3.1 eV in LiGaO_2 and 1.0 eV in NaGaO_2 .

I. INTRODUCTION

LiGaO_2 is a transparent ceramic material which has been considered for piezoelectric[1–3] and non-linear optical applications [4, 5] in the past and can be grown in bulk single crystal form,[6, 7] which has among other led to its use as closely lattice matched substrate[8–10] for GaN epitaxial growth. It can be viewed as a I-III-VI₂ analog of the II-VI material ZnO with a wurtzite based crystal structure, consisting of an ordered arrangement of the Li and Ga atoms on the cation sublattice of the wurtzite. In particular it has the $Pna2_1$ spacegroup. Mixed alloy systems of ZnO and LiGaO_2 and $\text{ZnO}/\text{LiGaO}_2$ heterojunctions have also been studied.[11–13]

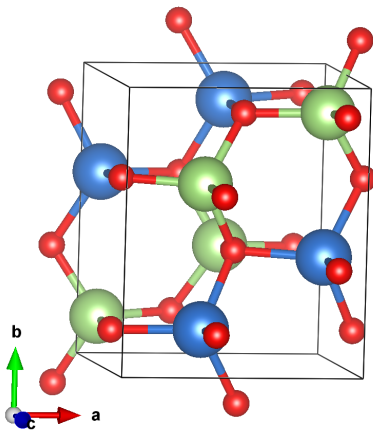
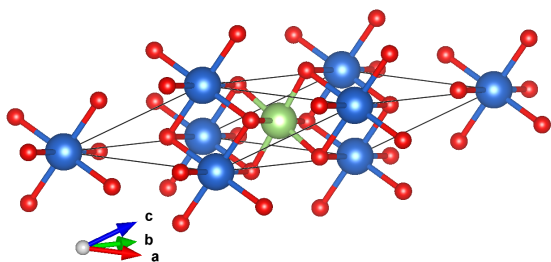
Although mostly considered an insulating material, it has recently been proposed that LiGaO_2 can be doped n-type with Si or Ge, which would make it promising for ultrawide gap semiconductor applications.[14–18] From this point of view it may have some advantages relative to the now widely pursued $\beta\text{-Ga}_2\text{O}_3$. [19, 20] It has a simpler crystal structure with all atoms tetrahedrally coordinated and it appears to have an even wider band gap.

However, the band gap is not yet fully established. While experiments indicate a gap of about 5.3-5.6 eV, a prior GW calculations predicted an even larger gap of 6.25 eV.[14] Optical absorption data give a direct gap of 5.5 eV [13, 21] to 5.26 eV [22] while X-ray absorption and emission data [23] gives a gap of 5.6 eV. Boonchun and Lambrecht[14] tried to explain their band gap overestimate compared to experiment in terms of tempera-

ture dependence of the gaps and zero-point motion correction by electron-phonon coupling. However, at that time no accurate predictions of these effects were possible. Since then, we have found in various other systems that \mathbf{k} -point and basis set convergence can significantly affect the QSGW band gap results.[24, 25] In this paper we re-evaluate the band structure of LiGaO_2 with well-converged quasiparticle self-consistent GW calculations and review the estimates of the electron-phonon coupling effects.

Secondly, we consider a related material of the same family, NaGaO_2 to evaluate the possibility of band gap tuning by varying the alkali metal component. One of the practical problems found in the past with LiGaO_2 as substrate is the ionic mobility of Li, which tends to easily diffuse. In particular for high-power applications with at high temperature or in the presence of strong electric fields, ion mobility might be expected to be a problem. Therefore replacing it by a less diffusive element Na might be beneficial. Indeed one of the main attractive features of ultrawide gap semiconductors is their large breakdown field. But then we also need to ensure that these high fields do not lead to ionic diffusion or loss of Li from the system.

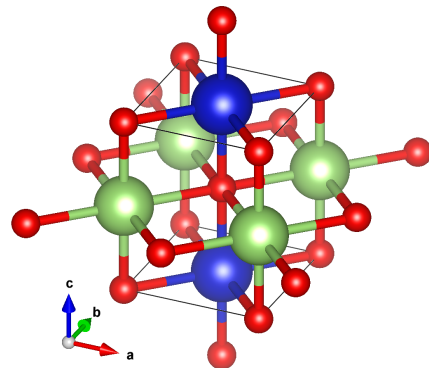
The known ground state structure of LiGaO_2 is the $Pna2_1$ structure,[6] for which the prototype is $\beta\text{-NaFeO}_2$. This structure is shown in Fig. 1. In this standard setting of the space group, $b > a > c$ with $b \approx 2a_w$, $a \approx \sqrt{3}a_w$ and $c = c_w$ in relation to the wurtzite hexagonal lattice constants. Note that in some previous literature,[3] the lattice constants a and b are reversed, $a > b > c$ in which

FIG. 1: $Pna2_1$ crystal structure.FIG. 2: $R\bar{3}m$ crystal structure.

case the space group setting is $Pbn2_1$. The notation n corresponds to a glide mirror plane with two glides, a or b to a glide plane with one glide along the indicated direction, so in the $Pna2_1$ notation n is in the bc plane and a in the ac plane and in both cases 2_1 indicates a two-fold screw-axis along c .

However, it is also worthwhile to study the competing α - NaFeO_2 structure, which has spacegroup $R\bar{3}m$ and is shown in Fig. 2. In that structure, all atoms are octahedrally coordinated and the structure can be viewed as a layered structure. According to the Materials Project (MP)[26] this structure has higher energy than the $Pna2_1$ structure for LiGaO_2 by 61 meV/atom. These results are obtained within density functional theory (DFT) in the Perdew-Burke-Ernzerhof (PBE) [27] generalized gradient approximation (GGA) approach and using high-throughput calculations. While providing important guidance, it is still important to check these results carefully for accuracy of small relative energy differences. This structure is commonly found in many ABO_2 systems with metallic elements functioning as cations. For example this structure is found for LiCoO_2 , a well known battery material, in which the Li content can to some extent be varied by chemical or electrochemical means.

It is important to check the relative stability of the two structures and determine the energetic preference for oc-

FIG. 3: $P4/mmm$ distorted rocksalt based structure with ordering of Li and Ga atoms in successive (001) planes.

tahedral vs. tetrahedral coordination of the Ga and alkali elements Li and Na. We therefore here also study the $R\bar{3}m$ band structures and relative stability of the two structures. In LiGaO_2 , disordered rocksalt phases have also been reported and these are also considered here. More specifically, instead of the disordered rocksalt phase, which would require averaging over a random arrangement of Li and Ga atoms on the cation sublattice of the cubic rocksalt phase, we use a simpler ordered arrangement of Li and Ga in alternating (001) planes of the face centered cubic cation sublattice, which then has spacegroup $P4/mmm$ and is shown in Fig. 3.

Finally, besides the electronic band structure, which is here provided in more detail than in Ref. 14, we also study the interband transition response functions related to optical absorption.

II. COMPUTATIONAL METHODS

The calculations in this work are done using the full-potential linearized muffin-tin orbital (FP-LMTO) all-electron method within either density functional theory (DFT) or many-body-perturbation theory (MBPT) context. The FP-LMTO method is used as implemented in the *questaal* package,[28, 29] and based on the work by Methfessel *et al* [30] and since then improved to allow for inclusion of augmented plane waves as additional basis functions,[31] which allows for a systematic check of the basis set convergence. We start our calculations from the structures available at the Materials Project (MP) [26] and then check the smallness of the residual forces within FP-LMTO or further relax the atomic positions within the cell. For materials not yet available in MP, we used the Quantum Espresso code [32] to relax the atomic positions and lattice constants simultaneously before additional testing with FP-LMTO. As DFT functional, we use the PBE-GGA[27].

A main advantage of the *questaal* package is that it has one of the few all-electron implementations of the

GW MBPT method. Here G and W refer to the one-particle Green's function and screened Coulomb interaction W , [33, 34] which define the self-energy operator $\Sigma = iGW$ in a schematic notation. Furthermore, this implementation uses a mixed-product-interstitial-plane-wave basis instead of only plane waves to represent all two-point quantities, such as the bare Coulomb interaction v , screened Coulomb interaction $W = \varepsilon^{-1}v = [1 - vP]^{-1}v$, polarization propagator P and inverse dielectric response function ε^{-1} . This representation is far more efficient to represent the response and does not require one to include as many high-energy empty bands for convergence. Details of the GW implementation can be found in Kotani *et al* [35] and Ref. 29.

The GW method is here used in the quasiparticle self-consistent version, known as QSGW. In this approach, the energy dependent $\Sigma(\omega)_{ij}$ is replaced by an energy-independent Hermitian average $\tilde{\Sigma}_{ij} = \frac{1}{2}\text{Re}[\Sigma_{ij}(\epsilon_i) + \Sigma_{ij}(\epsilon_j)]$, represented in the basis of initial H^0 eigenstates, where H^0 is the DFT starting Hamiltonian. The $\tilde{\Sigma}_{ij} - v_{xc}^{DFIT}$ is then added to the H^0 Hamiltonian in each iteration, providing a new G^0 Green's function from which a new W^0 and $\Sigma^0 = iG^0W^0$ is obtained in the next step. At convergence, the eigenvalues of the Kohn-Sham Hamiltonian H^0 are equal to the quasiparticle energies. Hence the name *quasiparticle self-consistent*. In other words, we are here focused on obtaining the real *quasiparticle energies*, independent of the DFT starting point, rather than the full energy dependent complex self-energy or Green's function which would contain a more comprehensive description of the quasiparticle spectral function.

Thanks to the atom-centered LMTO basis set, to which the self-energy can be converted, a natural route to interpolating the self-energy eigenvalue shifts to other \mathbf{k} -points than the mesh on which $\tilde{\Sigma}(\mathbf{k})_{ij}$ is calculated is available. In fact, it means that one can do a Fourier transform to represent the self-energy in real space $\tilde{\Sigma}_{\mathbf{R}L, \mathbf{R}'+\mathbf{T}L'}$ and then Fourier transform back to any \mathbf{k} -point desired. Here \mathbf{R} label atoms in the cell, \mathbf{T} is the translation vector defining the unit cell, and L includes angular momentum, lm , and other labels specifying the muffin-tin orbital basis functions. This is essentially equivalent to a Wannier function interpolation. Hence GW -accuracy energy bands and effective masses are obtained along the symmetry lines, or, on a fine mesh for density of states or optical response functions, without the need for the computationally expensive evaluation of $\tilde{\Sigma}(\mathbf{k})_{ij}$ on an equally fine mesh. Nonetheless, the \mathbf{k} -mesh on which the GW self-energy is determined is important for convergence. One finds that a coarse mesh tends to give larger band gaps.[24, 35, 36] Also important are a large basis set including typically *spdf - spd* angular momentum channels for two sets of smoothed Hankel function envelopes of the LMTOs as well as additional local orbitals to represent either semi-core states or higher lying conduction band contributions to the partial waves of the same angular momentum character within

the muffin-tin sphere partial.

We here used $3 \times 3 \times 3$ and $4 \times 4 \times 4$ \mathbf{k} -meshes on which the $\tilde{\Sigma}$ is calculated for the $Pna2_1$ structure to check convergence and a $6 \times 6 \times 6$ mesh for the $R\bar{3}m$ and $P4/mmm$ structures.

The QSGW method has been found to be significantly more reliable than the more prevalent G^0W^0 method because it does not depend on the starting H^0 but has been found to systematically overestimate the gaps. This has been largely found to be attributable to the underestimate of screening of the W . In fact, the electronic contribution to the macroscopic static dielectric constant has been found to be typically underestimated by 20 %.[37] Thus, the earlier introduced approach[38, 39] of using a fixed independent of material correction factor using only 80 % of $\Sigma - v_{xc}^{LDA}$ known as the 0.8Σ approach has been justified for not only typical semiconductors but even various transition metal oxides. The underlying physical reason is the neglect of electron-hole interaction effects in the random phase approximation calculation of W . When ladder-diagrams are included via a Bethe-Salpeter-Equation (BSE) approach[40] in the calculation of W , this 80% correction factor is no longer needed and it further helps justify the 0.8Σ correction. While the BSE approach is of course preferable being more fully first-principles, it is significantly more demanding computationally and for the materials considered here with 16 atoms per cell, it is still prohibitive. Guided by the success of the 0.8Σ approach in various related semiconductors, we also adopt it here.

III. RESULTS

A. Structural properties and stability of LiGaO₂

We start by examining the calculated and experimental structural parameters of LiGaO₂ in the $Pna2_1$ structure in Table I. This table also shows which symmetry operations link the different equivalent atoms of the $4a$ Wyckoff position. Here, 2_{1z} is the twofold screw axis along z located at the origin. The n_x is a double glide plane perpendicular to x and with glides by $b/2$ and $c/2$ which occurs at $x = \frac{1}{4}$ and therefore also involves a shift by $a/2$. The a_y is a single-glide plane perpendicular to y with shift by $a/2$ but it occurs at $y = 1/4$ and hence also involves a shift by $b/2$. Here the Cartesian axes x, y, z are chosen along a, b, c respectively.

We here compare the experimental structural parameters with the calculated ones within the PBE-GGA density functional from Materials Project.[26] The reduced coordinates within that model were verified using the FP-LMTO method and agree to ± 0.001 . We can see that PBE overestimates each of the lattice constants by about 1 % and hence the volume by 3 %. Interestingly, it overestimates Ga-O bond lengths slightly more than Li-O bond lengths. Also it overestimates c by about 1.4 % and a and b by about 0.8 %. Each cation has four different bond

TABLE I: Wyckoff positions and symmetry operation linking equivalent sites, lattice constants, volume per formula unit, reduced coordinates and bond lengths for LiGaO₂ in *Pna2*₁ structure, comparing expt. data from Ref. 6 with PBE-GGA relaxed structure.

4a positions operation	x, y, z 1	$-x, -y, z + \frac{1}{2}$ 2_{1z}	$\frac{1}{2} - x, y + \frac{1}{2}, z + \frac{1}{2}$ n_x	$x + \frac{1}{2}, \frac{1}{2} - y, z$ a_y
Expt. [6]				
a (Å)	b (Å)	c (Å)	V/fu (Å ³)	
5.407	6.405	5.021	43.471	
$2a/b$	$2c/b$	$b/2$		
1.6884	1.5678	3.2025		
atom	Wyckoff	x	y	z
Li	4a	0.0793	0.6267	-0.0064
Ga	4a	0.0821	0.1263	0.0000
O _{Li}	4a	0.0934	0.6388	0.3927
O _{Ga}	4a	0.0697	0.1121	0.3708
bond lengths (Å)				
Ga-O _{Ga} ^c	Ga-O _{Ga} ^a	Ga-O _{Li} ^a	Ga-O _{Li} ^b	
1.865	1.851	1.837	1.858	
Li-O _{Li} ^c	Li-O _{Li} ^a	Li-O _{Ga} ^a	Li-O _{Ga} ^b	
2.007	2.005	1.998	1.957	
GGA-PBE[26] and present calc.				
a (Å)	b (Å)	c (Å)	V/fu (Å ³)	
5.4665	6.4570	5.094	44.952	
$2a/b$	$2c/b$	$b/2$		
1.6932	1.5778	3.228		
atom	Wyckoff	x	y	z
Li	4a	0.0823	0.6244	0.0001
Ga	4a	0.0811	0.1261	0.0046
O _{Li}	4a	0.0928	0.6382	0.3959
O _{Ga}	4a	0.0688	0.1125	0.3726
bond lengths (Å)				
Ga-O _{Ga} ^c	Ga-O _{Ga} ^a	Ga-O _{Li} ^a	Ga-O _{Li} ^b	
1.878	1.877	1.868	1.870	
Li-O _{Li} ^c	Li-O _{Li} ^a	Li-O _{Ga} ^a	Li-O _{Ga} ^b	
2.019	2.018	2.016	1.998	

lengths to oxygen, for example Ga-O_{Li}^a means the bond length between Ga and the O_{Li} type O in the *a*-direction. We can see that the Li-O bond lengths are significantly larger than the Ga-O bond lengths. The $2a/b$ ratio in the undistorted wurtzite structure derived *Pna2*₁ structure would be $\sqrt{3} \approx 1.732$, but here is reduced to 1.69. This implies that the 120° angle between two wurtzite lattice vectors in the plane has here increased to 122°.

Next, we discuss the structural stability relative to the *R* $\bar{3}m$ structure. Note that in the *R* $\bar{3}m$ structure, the cations have octahedral coordination and form a layered structure with alternating Li and Ga containing layers. We start again from the structural parameters of the Materials Project,[26] which are optimized within the GGA-PBE density functional. The structural parameters of *R* $\bar{3}m$ are given in Table II. Clearly, the volume per formula unit in this structure is significantly (18 %) lower than in the *Pna2*₁ structure, meaning that this phase can be stabilized under pressure. Interestingly, both Ga-O and Li-O bond lengths are larger in the octahedral environment. This structure is known as α -LiGaO₂ and

its structure was determined by Marezio and Remeika [41].

Yet, another form of LiGaO₂ is known as γ -LiGaO₂ and has a rocksalt-like structure with tetragonal distortion. In this phase, LiGaO₂ is also octahedrally coordinated and the Li and Ga occur in a disordered way in the Wyckoff *2b* positions of space group *I4/m* with equal probability. Instead, a closely related structure, *P4/mmm* is considered in MP[26]. This is an ordered distorted rocksalt modification as shown in Fig. 3 and already discussed in Sec. I. The lattice constants and atomic positions of this phase from MP[26] are given in Table III. Note that in this structure the Li-O and Ga-O bond lengths are fixed to be $a\sqrt{2}/2$ perpendicular to *c* and $c/2$ parallel to *c*. This is unfavorable from the point of view that the bond lengths cannot be individually optimized for each species. The experimental *I4/m* disordered rocksalt-like structure according to Lei *et al* [42] has lattice constants of $a = 2.8763$ Å and $c = 4.1929$ Å and hence $c/a = 1.4577$, close to the ideal $\sqrt{2} = 1.4142$. In contrast, the c/a ratio in *P4/mmm* is

TABLE II: Structural parameters of LiGaO₂ in $R\bar{3}m$ structure.

	Li	Ga	O
Wyckoff	1a	1b	2c
reduc. coord.	(0, 0, 0)	($\frac{1}{2}, \frac{1}{2}, \frac{1}{2}$)	($\pm u, \pm u, \pm u$)
Calculated			
$a = b = c$ (Å)	$\alpha = \beta = \gamma$	V/fu (Å ³)	u
5.173	33.138°	36.824	0.2415
bond lengths (Å)	Li-O	Ga-O	
	2.171	2.026	
Experiment[41]			
$a = b = c$ (Å)	$\alpha = \beta = \gamma$	V/fu (Å ³)	u
5.1066±0.0005	33.12°	35.394	0.2417
bond lengths (Å)	Li-O	Ga-O	
	2.14	2.00	

TABLE III: Lattice constants and atomic positions of LiGaO₂ in $P4/mmm$ structure.

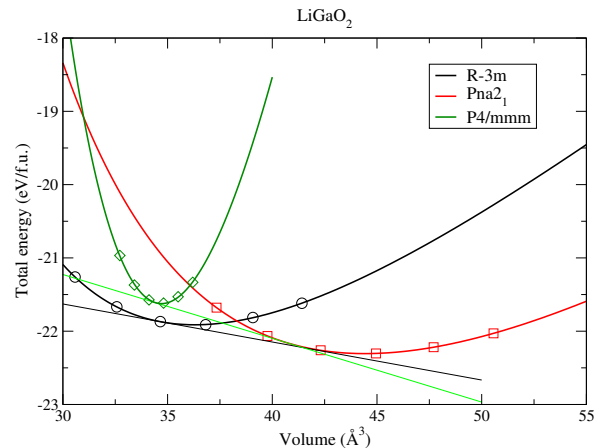
atom	Wyckoff	x	y	z
Li	1c	0.5	0.5	0.0
Ga	1b	0.0	0.5	0.0
O	1a	0.0	0.0	0.0
O	1d	0.5	0.5	0.5
lattice constants (Å)	$a = b$	c	V/fu	
	3.002	3.861	34.807	
bond lengths (Å)	$\parallel c$	$\perp c$		
	1.930	2.123		

TABLE IV: Cohesive energy ($E_0/f.u.$), equilibrium volume (V_0), bulk modulus (B_0) and its pressure derivative (B'_0) and transition pressure, p_t from $Pna2_1$ to other phase for LiGaO₂.

property	$R\bar{3}m$	$Pna2_1$	$P4/mmm$
V_0 (Å ³)	36.297	44.424	34.712
E_0 (eV/f.u.)	21.91	22.30	21.62
B_0 (GPa)	166	130	1615
B'_0	4.6	4.2	5.0
p_t (GPa)	8.3		13.9

reduced to 1.286. Following Lei *et al* [42] a disordered cubic rocksalt phase with space group $Fm\bar{3}m$ also exists and is designated as δ -LiGaO₂. It has a lattice constant of 4.1134 Å. All these phases have close volumes per formula unit of about 34.8 ± 0.1 Å³.

We calculated the total energies of the $Pna2_1$, $R\bar{3}m$ and $P4/mmm$ phases as function of volume, keeping the ratios of the lattice constants (shape of the cell) and internal parameters fixed within the GGA-PBE functional with the FP-LMTO method. In order to compare the energies accurately, we used the same muffin-tin radii for the three structures, chosen to be touching in the $Pna2_1$ structure at 0.94 compression of the lattice constants.

FIG. 4: Energy volume curves of LiGaO₂ in $R\bar{3}m$, $P4/mmm$ and $Pna2_1$ phases and the common tangent constructions. The data points are directly calculated, the lines are Murnaghan equation of state fits.

This avoids overlap of the spheres in the other structures. We included augmented plane waves in the basis set up to 3 Ry and used a large basis set $spdf - spd$ on Li and Ga and also included the Ga-3d semi-core states as bands. We found the energy difference between the $R\bar{3}m$ and $Pna2_1$ phases at their equilibrium volume to be converged to 0.1 eV by increasing the cut-off of the augmented plane waves to 4 Ry.

The energy-volume curves and common tangent constructions are shown in Fig.4. The energy volume curves were fitted to the Murnaghan equation of state and the latter was used to determine the transition pressure from the common-tangent rule or equivalently, setting the enthalpy, $H_i(p) = E_i[V_i(p)] + pV_i(p)$ equal for two different phases i . The equation of state fitted parameters are given in Table IV. The energy difference between

the $Pna2_1$ and $R\bar{3}m$ phases amounts to 97.5 meV/atom which is somewhat larger than the value given in MP[26] of 61 meV. The $P4/mmm$ phase is found to have higher energy than the $R\bar{3}m$, namely 170 meV/atom higher than the $Pna2_1$ phase but occurs at minimum energy volume of 34.7 \AA^3 close to that of the $R\bar{3}m$ phase. The bulk moduli might be somewhat overestimated because we did not allow the structure to relax at each volume. Prior work found a bulk modulus of ~ 95 GPa for the $Pna2_1$ structure[3, 43] and 142.29 GPa in $R\bar{3}m$. [43]

Phase transitions of the β -LiGaO₂ $Pna2_1$ to the α form $R\bar{3}m$ and other disordered rocksalt type forms have been studied by Raman spectroscopy.[42, 43] At 14 GPa a transition is found to the $I4/m$ structure, which is closely related to the rocksalt structure. This is very close to our value of the transition to the $P4/mmm$ phase. According to Lei *et al* [43], the α -phase can be prepared from the β -phase at 7 GPa and 1000°C. This is compatible with the transition pressure found here between the $Pna2_1$ and $R\bar{3}m$ phase of 8.3 GPa. From our convergence studies we estimate our value to have an uncertainty of a few GPa, in particular because we calculated our energy-volume curves without relaxing the internal parameters or shape of the cell. Our calculations predict that the transition to $R\bar{3}m$ should occur first. This agrees qualitatively with the phase diagram as function of temperature and pressure presented by Lei *et al* [42] in which the $R\bar{3}m$ phase occurs at lower pressure than the cubic rocksalt phase or the lower temperature $I4/m$ phase. Their explanation for the transition to the $I4/m$ phase is that kinetic reasons could prevent the transition from $Pna2_1$ to $R\bar{3}m$ at low temperature (in other words there is insufficient driving force and thermal activation) and as the pressure is then further increased, the phase transition when finally triggered, may then proceed already to the tetragonally distorted rocksalt type phase, which only is stable at higher pressures.[43]

B. Band structure of LiGaO₂ in $Pna2_1$ structure

For our band structure investigations of LiGaO₂ in the $Pna2_1$ structure, we used the experimental lattice parameters and atomic positions from Marezio *et al* [6]. For completeness they are given in Table I.

The band structure of LiGaO₂ in QSGW 0.8Σ is shown on a large energy scale in Fig. 5. The density of states resolved in various partial densities of state (PDOS) are shown in Fig. 6 both in the conduction band and the valence band region. This shows that the lowest set of narrow bands at about -19 eV are the O-2s derived bands and the ones at about -12 eV below the VBM are the Ga-3d derived bands. The next set of bands between -6 eV and 0 eV are the O-2p dominated band. In the conduction bands we see also significant oxygen contributions because these are antibonding bands. It shows that the conduction band minimum has more Ga-4s contribution and the main Li-2s only occurs at significantly

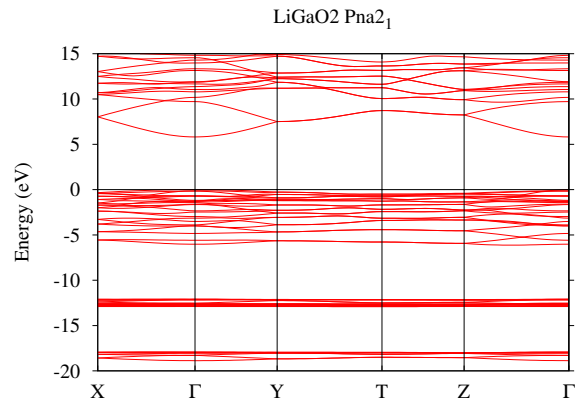


FIG. 5: Band structure LiGaO₂ in $Pna2_1$ structure in 0.8Σ QSGW approximation.

TABLE V: Character table of point group C_{2v} indicating both the chemistry and Koster notation of the irreducible representations.

chem	Koster	1	2_{1z}	n_x	a_y	functions
a_1	Γ_1	1	1	1	1	z, x^2, y^2, z^2
a_2	Γ_3	1	1	-1	-1	xy
b_1	Γ_4	1	-1	-1	1	x, xz
b_2	Γ_2	1	-1	1	-1	y, yz

higher energy, above 18 eV. This is consistent with the high electropositivity of Li. This can also be seen in the colored band plot in Fig. 7.

Next we show a zoom in on the region near the conduction band minimum and valence band maximum in Fig. 8. The bands are symmetry labeled according to the character table given in Table V, following the Koster *et al* [44] notation. The band gap is direct at Γ and is 5.81 eV. The conduction band minimum (CBM) is found at Γ and shows a strongly dispersive band with low effective mass as is typical for cation- s -like CBMs. The valence band maximum (VBM) is also at Γ but shows crystal field splitting compared to the three-fold degenerate p -like state seen in cubic zincblende materials. Compared to wurtzite which has only z split from x, y states, there is here a full splitting in three levels even without spin-orbit coupling.

We can see that the CBM has Γ_1 symmetry, consistent with its dominant s -like character. The VBM also has Γ_1 symmetry, separated by 124 meV from the Γ_4 band and the latter separated by 48 meV from the next Γ_2 . Since $\Gamma_1, \Gamma_4, \Gamma_2$ correspond to z, x, y respectively, this implies that optical transitions from the Γ_1 VBM to the CBM are dipole allowed for $\mathbf{E} \parallel \mathbf{c}$, from the Γ_4 band for $\mathbf{E} \parallel \mathbf{a}$ and for the Γ_2 band for $\mathbf{E} \parallel \mathbf{b}$. These lead to different onsets of absorption as confirmed by our calculations of the optical response discussed below.

Along the $\Gamma - X$ direction, only the a_y mirror symmetry leaves the \mathbf{k} -point invariant and the states can thus

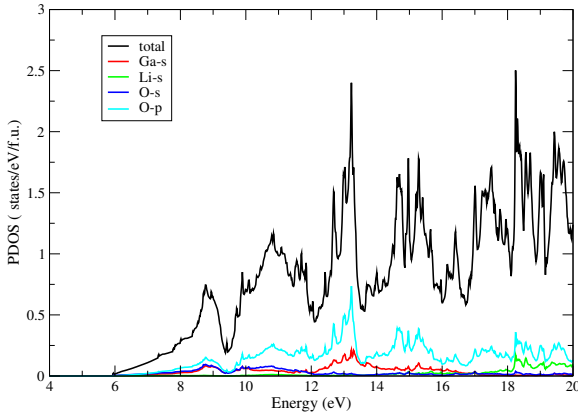
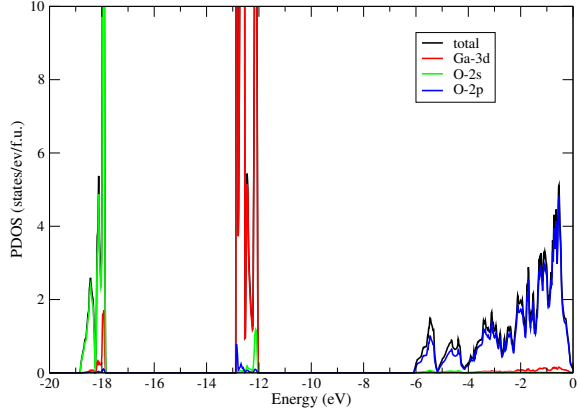


FIG. 6: Total and partial densities of states for valence band (top) and conduction band (bottom) region.

be labeled as even, +, or odd, $-$, with respect to that mirror plane. From the character table, one can easily see that Γ_1 and Γ_4 are compatible with + and Γ_2, Γ_3 are compatible with $-$ along this direction. Therefore the second and third valence band (counting down from the top) are allowed to cross along $\Gamma - X$. Likewise along $\Gamma - Y$, only the n_x mirror survives. The compatibility relations are now $\{\Gamma_1, \Gamma_2\} \rightarrow +$, $\{\Gamma_3, \Gamma_4\} \rightarrow -$. On the other hand, along $\Gamma - Z$ the group of \mathbf{k} stays C_{2v} and hence the symmetry labeling at Γ also applies along the $\Gamma - Z$ axis. Since the top three bands have different symmetry label they are allowed cross along this line.

In the conduction band we have only labeled the bands at Γ since the labels along the three orthogonal directions from Γ is already clear from the previous paragraph. We can see that there is a large gap of 3.90 between the CBM and next conduction band (CBM2), which is of Γ_4 symmetry. This is favorable for transparent conductor applications since only light with photon energy larger than

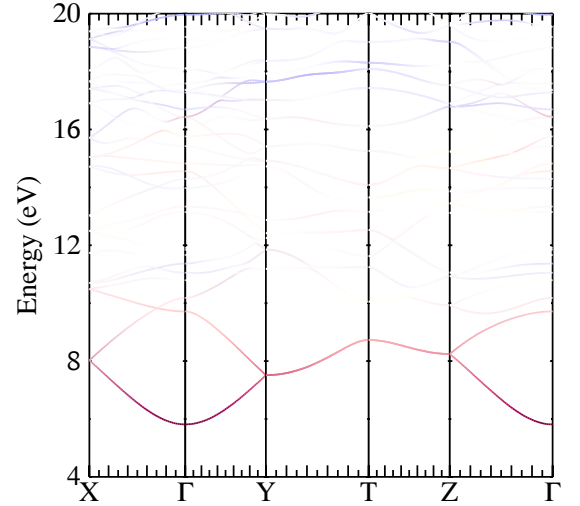


FIG. 7: Conduction band structure of LiGaO_2 in $Pna2_1$ structure in 0.8Σ approximation showing the Ga-4s in red and Li-2s in blue contributions to the bands.

TABLE VI: Effective masses (in units of the free electron mass) in $Pna2_1$ LiGaO_2 and energy levels at Γ relative to the VBM.

band	irrep	E (eV)	m_x	m_y	m_z
CBM	Γ_1	5.81	0.39	0.39	0.41
VBM1	Γ_1	0	3.85	3.50	0.42
VBM2	Γ_4	-0.124	0.45	3.50	3.80
VBM3	Γ_2	-0.172	3.15	0.58	3.80

3.9 eV (wavelength $\lambda < 318$ nm) and with polarization $\mathbf{E} \parallel \mathbf{a}$ would be absorbed by electrons near the conduction band minimum introduced by n-type doping. The next CBM3 has Γ_3 symmetry which is dipole forbidden for any light polarization. The first allowed transitions from the CBM for $\mathbf{E} \parallel \mathbf{b}$ would only occur to the CBM4 band of Γ_2 symmetry at 4.98 eV. The lowest conduction band at Γ of Γ_1 symmetry is CBM7 at 5.85 eV.

Because of the orthorhombic symmetry the mass tensors at each band at Γ are diagonal with a different mass in each of the x, y, z directions. These are given in Table VI. One can see that the conduction band mass is small and close to isotropic. The valence bands each have one light mass and two heavy mass directions. The light mass is in the direction corresponding to the symmetry of the band, for example it is in the x direction for the Γ_4 band, in the y direction for the Γ_2 band and in the z direction for the Γ_1 band.

We also performed calculations including spin-orbit coupling. The valence band maximum is then still split in three levels and the difference from the calculation without spin-orbit coupling was found to be negligible. In the parent compound ZnO , spin-orbit splitting plays an important role because of the antibonding contribution

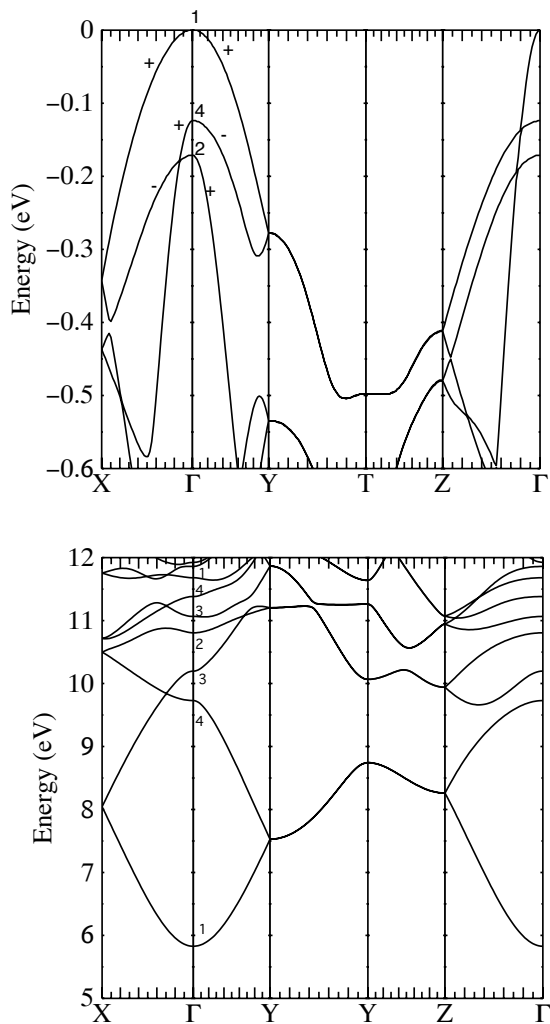


FIG. 8: Symmetry labeled bands. Please note different scales in (top) near valence band maximum) and (bottom) conduction band region.

from the Zn-3d orbitals in the VBM. In fact, it leads to an effectively negative spin-orbit splitting parameter of the VBM in that case.[45] In LiGaO₂, however the Ga-3d orbitals lie significantly lower, reducing this negative contribution and hence apparently almost completely cancelling the positive but already small contribution of the O-2p orbitals.

The optical response functions were calculated within the long-wavelength limit and independent particle approximation. In other words, they include vertical band-to-band transitions including the dipole matrix elements but no local field or excitonic effects. In this case the imaginary part of the dielectric function $\varepsilon_2(\omega)$ is given by

$$\varepsilon_2(\omega) = \frac{8\pi^2 e^2}{V\omega^2} \sum_n \sum_{n'} \sum_{\mathbf{k} \in BZ} f_{n\mathbf{k}}(1 - f_{n'\mathbf{k}}) |\langle \psi_{n\mathbf{k}} | [H, \mathbf{r}] | \psi_{n'\mathbf{k}} \rangle|^2 \delta(\omega - \epsilon_{n'\mathbf{k}} + \epsilon_{n\mathbf{k}}), \quad (1)$$

TABLE VII: Dielectric constants ε^∞ of LiGaO₂ in various approximations.

method	ε_x^∞	ε_y^∞	ε_z^∞	$(\varepsilon_x^\infty \varepsilon_y^\infty \varepsilon_z^\infty)^{1/3}$
LDA[3] Berry	3.492	3.342	3.490	3.441
GGA	2.803	2.750	2.824	2.792
0.8 Σ $d\Sigma/dk$	4.987	5.421	7.256	5.810
0.8 Σ $d\Sigma/dk = 0$	1.818	1.796	1.828	1.810
0.8 Σ rescaling	2.445	2.399	2.462	2.435
Expt. [46]	2.99	2.90	2.99	2.960
Expt. [1]	3.05	2.99	3.05	3.030

with $\epsilon_{n\mathbf{k}}$ the band eigenvalues, $\psi_{n\mathbf{k}}$ the Bloch eigenstates, $f_{n\mathbf{k}}$ the Fermi function occupation factors of these states. It uses matrix elements of the velocity operator $\dot{\mathbf{r}} = (i/\hbar)[H, \mathbf{r}]$, which differ from the momentum matrix elements \mathbf{p}/m because of the non-local contribution of the self-energy operator to the Hamiltonian. The real part $\varepsilon_1(\omega)$ is obtained from a Kramers-Kronig transformation and the optical absorption coefficient is given by $\alpha(\omega) = 2\varepsilon_2(\omega)/n(\omega)$ with $n(\omega)$ the index of refraction given by $\tilde{n}(\omega) = \sqrt{\varepsilon_1(\omega) + i\varepsilon_2(\omega)} = n(\omega) + i\kappa(\omega)$.

The imaginary and real parts of the dielectric function are shown in Fig. 9 and the absorption coefficient is shown on a log scale near the onset of absorption in Fig. 10. It shows the different absorption onsets for different polarization consistent with the symmetry analysis present above.

The values of $\varepsilon_1(\omega = 0)_{\alpha\alpha}$ correspond to the ε^∞ and can be compared with the results obtained from a Berry-phase calculation in LDA in Boonchun and Lambrecht.[3] This comparison is given in Table VII along with our values both based on the GGA and the QSGW 0.8 Σ band structure. The Berry phase calculations in principle includes local field corrections which tend to reduce the value by about 5 %. In spite of this our GGA values are smaller than the ones in Ref. 3. The increase in gap due to QSGW is expected to reduce the dielectric constant (because energy denominators in the expression for ε are increased) when applied in a naive way without taking into account the matrix element rescaling, from the non-local contribution to the velocity operator from the self-energy. This is indicated in the table by the $d\Sigma/dk = 0$. However when including the $d\Sigma/dk$ contribution the dielectric constant is in fact increased compared with GGA. Instead of using the explicitly calculated $d\Sigma/dk$ one can also use the rescaling rule proposed by Levine and Allan [47] in the context of a scissor correction. One then rescales the matrix elements by a factor $(\epsilon_{n\mathbf{k}} - \epsilon_{n'\mathbf{k}})/(\epsilon_{n\mathbf{k}}^{GGA} - \epsilon_{n'\mathbf{k}}^{GGA})$. This apparently restores values close to the GGA. Finally, we compare to experimental values. Interestingly, the GGA results seem to be in better agreement with the experiment but we should caution that this could be due to a compensation of errors because we did not include local field or excitonic effects here.

Let us now focus on the band gap in Table VIII. First,

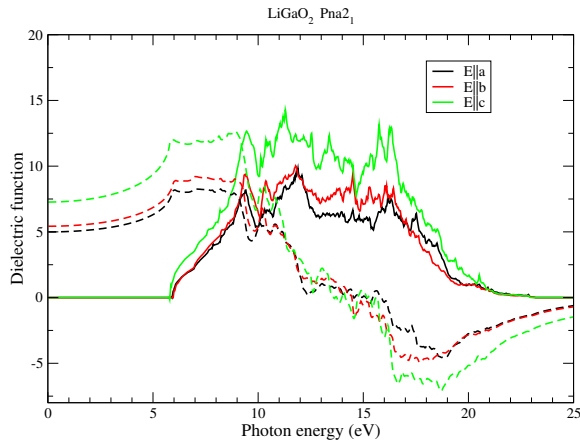


FIG. 9: Imaginary ϵ_2 and real ϵ_1 parts of the optical dielectric function for x, y, z directions.

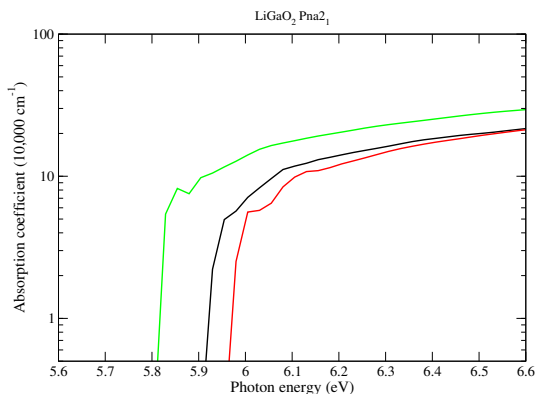


FIG. 10: Optical absorption onset $\alpha(\omega)$ for the three crystal directions.

in terms of \mathbf{k} -convergence of the $\tilde{\Sigma}(\mathbf{k})$, the 0.8Σ gap obtained with a $3 \times 3 \times 3$ mesh is 5.804 eV while that with a $4 \times 4 \times 4$ mesh it is 5.812 eV, showing that we have reached convergence to 0.01 eV in terms of \mathbf{k} -convergence. The full QSGW gaps are 6.35 and 6.36 eV with $3 \times 3 \times 3$ and $4 \times 4 \times 4$ respectively. One can see that the GW corrections to the GGA band structure are significant. Also, we find a gap of 5.8 eV in fair agreement with experiments

TABLE VIII: Band gap of LiGaO_2 in $Pna2_1$ structure in different approximations.

	GGA	QSGW	0.8Σ	+ZPM	Expt.
At expt. a, b, c	3.363	6.363	5.81	5.6	5.26-5.5
at PBE a, b, c	3.201	6.245	5.69	5.5	

when adding a 0.8 correction factor to the $\tilde{\Sigma} - v_{xc}^{DFT}$. This is known as the 0.8Σ approximation as discussed in Sec. II.

While a full calculation of the zero point motion correction to the gap by electron phonon coupling is time consuming, we can make at least some estimate of this effect following the approach of Ref. 48. In a highly ionic material, the main effect comes from the lattice polarization correction (LPC), which is essentially the polaronic shift of the band edges. Its origin can be viewed as the contribution to the screening from the lattice polarization in the long-wavelength limit. For a material with a single LO phonon, this shift is given by[48]

$$\Delta E_P = -\alpha_P \hbar \omega_{LO} / 2 = \frac{e^2}{4a_P} \left[\frac{1}{\epsilon_\infty} - \frac{1}{\epsilon_0} \right] \quad (2)$$

where $a_P = \sqrt{\hbar / (2\omega_{LO} m_*)}$ is a polaron length defined in terms of the effective mass of the electrons for the conduction band shift and holes for the valence band shift and ω_{LO} is the longitudinal optical phonon. The dimensionless polaronic coupling factor is α_P and the dielectric constants at frequencies high above the phonons but well below the gap is ϵ_∞ and the static dielectric constant below the phonon modes is ϵ_0 . The factor 1/2 in this equation was obtained by applying a cut-off to the wave vector integration over the electron-phonon coupling interaction of order $1/a_P$ while the classic Fröhlich estimate of the polaronic shift extends the integral to infinity.[48, 49] Whether this cut-off procedure should be used or not is still a matter of debate.[50] Hence our estimate may be underestimated by a factor two but we are only after an order of magnitude estimate. We obtain an upper limit to this correction by calculating the contribution from the highest energy optical phonon. The phonons in LiGaO_2 were calculated in Boonchun *et al* [3] and this paper also provides values for the dielectric constants needed here. Averaging over the b_{1L} , b_{2L} and a_{1L} phonons, we take an estimate of $\omega_{LO} \approx 750 \text{ cm}^{-1}$. Averaging the dielectric constants over directions, we obtain $\epsilon_\infty \approx 3.44$, $\epsilon_0 \approx 6.93$. The factor $[\epsilon_\infty^{-1} - \epsilon_0^{-1}]$ then amounts to 0.146. Now using a hole mass of about $m_* = 3$ we obtain $a_P^h \approx 7a_0$ with a_0 the Bohr radius. The expected shift is then about 0.14 eV. The conduction band shift should be significantly smaller because the electron effective mass is only 0.33 giving an $a_P^e \approx 21a_0$, giving a shift of 0.05 eV at most. This gives an estimated gap correction of -0.2 eV from the highest frequency LO phonons. When multiple infrared active phonons are present, each phonon has a separate contribution to the $\epsilon_0/\epsilon_\infty$ factor according to the Lyddane-Sachs-Teller relation but also each long-range Fröhlich type electron-phonon coupling parameter depends on the eigenvector of the phonon.[51] It does become much more difficult to make an estimate. The above should be viewed only as an order of magnitude estimate of the effect. Including this estimate of a negative shift of a few 0.1 eV of the electron phonon coupling zero-point motion correction, our gap is in excellent agreement with the experimen-

tal value. The remaining discrepancy of our value with the most recent experimental determination of 5.26 eV is probably due to this measurement being done at room temperature.

It is also of interest to check how the QSGW correction of the gap is split over the valence and conduction band edges. We find in the 0.8Σ approximation that the VBM shifts down from the GGA value by 1.321 eV while the CBM shifts up by 1.128 eV, thus giving a gap correction of 2.449 eV. This is related to the Ga-3d contribution to the VBM. The Ga-3d bands are found to shift down by about 2 eV in the 0.8Σ approximation compared to GGA. This reduces the antibonding contribution of the Ga-3d to the VBM and hence shifts down the VBM significantly. The O-2s bands also shift down by about 1.7 eV.

We note that at the PBE calculated lattice constants, the GGA gap is ~ 0.12 eV smaller. This is because the larger lattice constant typically leads to lower covalent interactions and hence a lower band gap. Since volume in GGA is about 3 % overestimated, this allows us to estimate the band gap deformation potential $dE_g/d\ln V \approx 4$ eV.

C. LiGaO₂ in $R\bar{3}m$ and $P4/mmm$ structures.

The band structure of the $R\bar{3}m$ structure of LiGaO₂ was calculated in the 0.8Σ QSGW approximation and is shown in Fig. 11. We use the symmetry line notation of Ref. 52 or the Bilbao Crystallography Server: <https://www.cryst.ehu.es/>. We can see that the band gap in this structure is slightly indirect, because the VBM occurs between Γ and S while the CBM remains at Γ . The direct gap at Γ is 5.65 eV while the indirect gap is 5.47 eV. The O-2s and Ga-3d bands occur at about the same energies as in the $Pna2_1$ structure.

The band structure in the $P4/mmm$ structure is shown in Fig 12 in the 0.8Σ approximation. It is seen to have a direct gap but with significantly smaller value of 3.129 eV.

D. Structure and stability of NaGaO₂

The structural parameters of $Pna2_1$ NaGaO₂ were initially taken from Materials Project and subsequently relaxed within the GGA-PBE approximation using the questaal and Quantum Espresso codes. They are given in Table IX. After we finished the calculations, we found that NaGaO₂ in the $Pna2_1$ structure has been synthesized and its lattice constants were reported by Weise and Neumann,[53] who quote even some earlier results. The experimental values are included here and show that the PBE-GGA as usual somewhat overestimates the lattice constants.

We see that the $2a/b$ is significantly smaller than the ideal value of $\sqrt{3}$, indicating that the γ angle between a and b has increased from 120° to 129° . The Na-O bond

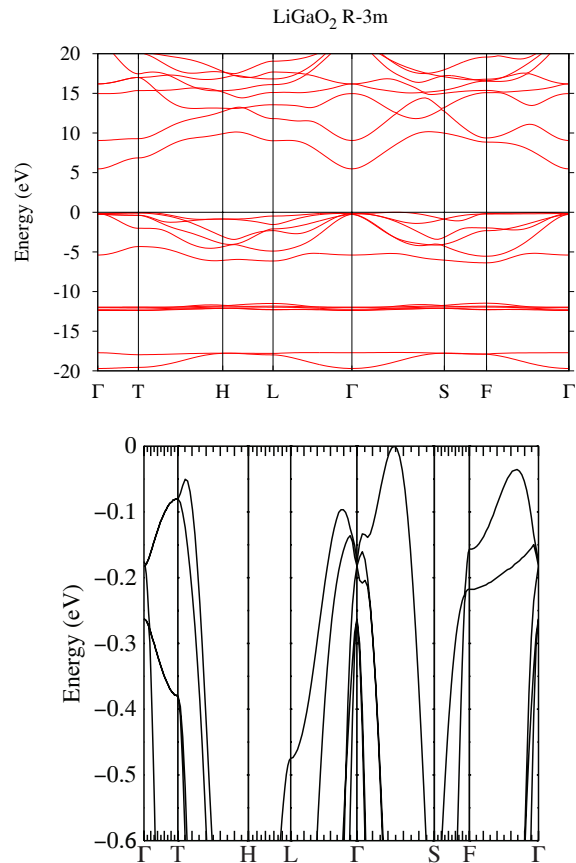


FIG. 11: Band structure of LiGaO₂ in the $R\bar{3}m$ structure in 0.8Σ QSGW approximation. Bottom shows zoom in on the VBM.

lengths are larger than the Li-O bond lengths while the Ga-O bond length is about the same as in LiGaO₂. As expected, the volume per formula unit is somewhat larger than in LiGaO₂.

The optimized structural parameters of the $R\bar{3}m$ structure are given in Table X. We find this structure to have a volume per formula unit that is 22% smaller than the $Pna2_1$ structure and to be 165 meV/atom higher in energy. It is thus again a high-pressure phase. Using the energy-volume curves shown in Fig. 13 we find a transition pressure of 13 GPa. This is comparable but slightly higher than in LiGaO₂. Both are close to the transition from wurtzite ZnO to rocksalt ZnO, which occurs at about 9 GPa. The $P4/mmm$ structure was optimized first as function of c/a and then the equation of state was determined keeping the c/a fixed. The Murnaghan fit parameters and transition pressure from the $Pna2_1$ phase are given in Table XII.

TABLE IX: Lattice constants, volume per formula unit, reduced coordinates, and bond lengths of NaGaO₂ in *Pna2*₁ structure optimized within GGA-PBE.

	a (Å)	b (Å)	c (Å)	V/fu (Å ³)
Present calculation	5.6138	7.2377	5.3895	54.746
Experiment [53]	5.495	7.221	5.297	52.545
	$2a/b$	$2c/b$	$b/2 = a_w$	
	1.5513	1.4893	3.6189	
atom	Wyckoff	x	y	z
Na	4a	0.0717	0.6223	0.0128
Ga	4a	0.0630	0.1262	-0.0005
O _{Na}	4a	0.1149	0.6632	0.5822
O _{Ga}	4a	0.0400	0.08923	0.6559
bond lengths (Å)				
Ga-O _{Ga} ^c	Ga-O _{Ga} ^a	Ga-O _{Na} ^a	Ga-O _{Na} ^b	
1.875	1.864	1.880	1.875	
Na-O _{Na} ^c	Na-O _{Na} ^a	Na-O _{Ga} ^a	Na-O _{Ga} ^b	
2.357	2.346	2.312	2.325	

TABLE X: Structural parameters of NaGaO₂ in $R\bar{3}m$ structure.

	Na	Ga	O
Wyckoff	1a	1b	2c
reduc. coord.	(0, 0, 0)	($\frac{1}{2}, \frac{1}{2}, \frac{1}{2}$)	($\pm u, \pm u, \pm u$)
$a = b = c$ (Å)	$\alpha = \beta = \gamma$	V/fu (Å ³)	u
5.675	30.892°	42.742	0.2326
bond lengths (Å)	Li-O	Ga-O	
	2.389	2.047	

TABLE XI: Lattice constants and atomic positions of NaGaO₂ in *P4/mmm* structure.

atom	Wyckoff	x	y	z
Na	1c	0.5	0.5	0.0
Ga	1b	0.0	0.5	0.0
O	1a	0.0	0.0	0.0
O	1d	0.5	0.5	0.5
lattice constants (Å)	$a = b$	c	V/fu	
	3.189	4.177	42.498	
bond lengths (Å)	$\parallel c$	$\perp c$		
	2.088	2.255		

TABLE XII: Cohesive energy ($E_0/f.u.$), equilibrium volume (V_0), bulk modulus (B_0) and its pressure derivative (B'_0) and transition pressure, p_t of NaGaO₂

property	$R\bar{3}m$	<i>Pna2</i> ₁	<i>P4/mmm</i>
V_0 (Å ³)	41.19	53.35	42.50
E_0 (eV/f.u.)	19.96	20.62	19.08
B_0 (GPa)	161	116	1047
B'_0	4.5	4.3	5.0
p_t (GPa)	13.0		40.0

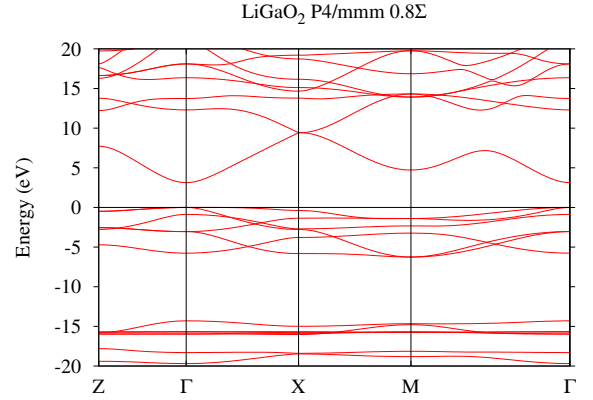


FIG. 12: Band structure of LiGaO₂ in the *P4/mmm* structure in 0.8 Σ QSGW approximation.

E. Band structure of NaGaO₂ in *Pna2*₁ structure

The large energy scale band structure of *PNa2*₁ NaGaO₂ is shown in Fig. 14. The partial densities of states in the valence and conduction band region are given in Fig. 15. They show similar to LiGaO₂ that the Ga-3*d* bands lie above the O-2*s* ones and that the Na contribution to the conduction band PDOS occurs mainly well above the conduction band minimum, while the latter is dominated by Ga-4*s*. This is also shown in Fig. 16 which shows the Ga-4*s* and Na-3*s* contributions to the conduction bands. In addition, the Na-2*p* semicore levels are seen to lie at about -25 eV.

A zoom in on the valence band maximum and conduction band minimum range are shown in Fig. 17. The band splittings of the VBM and corresponding effective mass tensor components are given in Table XIII. The band gap is only slightly lower than for LiGaO₂ with a value of 5.49 eV in the 0.8 Σ approximation and 2.88

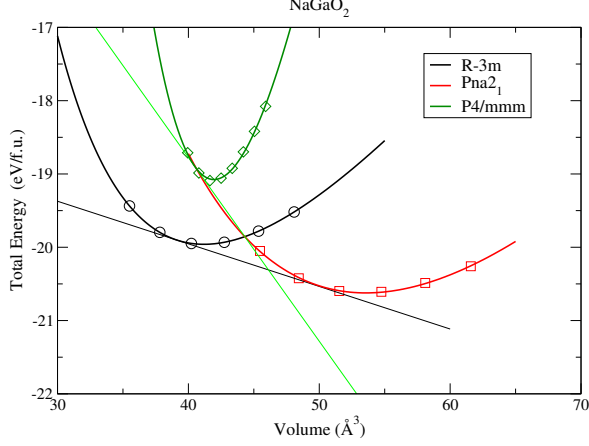


FIG. 13: Total energy of NaGaO₂ (minus the energy of the corresponding free atoms) as function of volume for *Pna*₂₁, *R3m* and *P4/mmm* structures and the common tangent constructions. Symbols are calculated, lines are Murnaghan equation of state fits.

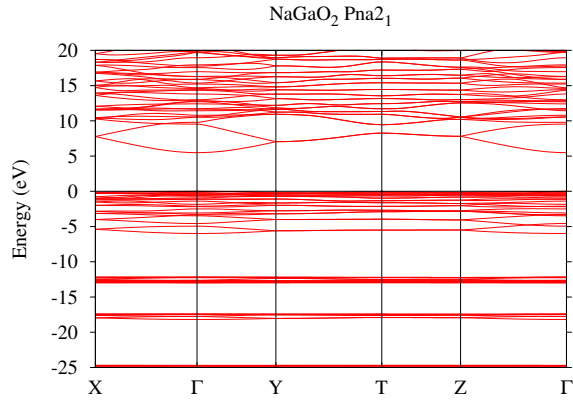


FIG. 14: Band structure NaGaO₂ in *Pna*₂₁ structure in 0.8Σ QSGW approximation.

eV in the GGA approximation. The shift of the individual band edges between GGA and 0.8Σ *GW* is -1.49 eV in the valence band and 1.12 eV in the conduction band. The band gap is probably still slightly overestimated because of the GGA overestimate of the lattice constant. Including a zero-point motion correction similar to LiGaO₂ and a lowering of gap by the deformation potential correction, we estimate that the gap is 5.1±0.1 eV, which is only slightly lower than in LiGaO₂ and still significantly higher than in β-Ga₂O₃.

The dielectric functions and optical absorption are given in Figs. 18,19. They confirm the analysis of the optical anisotropy of the absorption onset based on the symmetry labeled valence bands. An interesting difference from LiGaO₂ is that in NaGaO₂, the *x* and *z* polar-

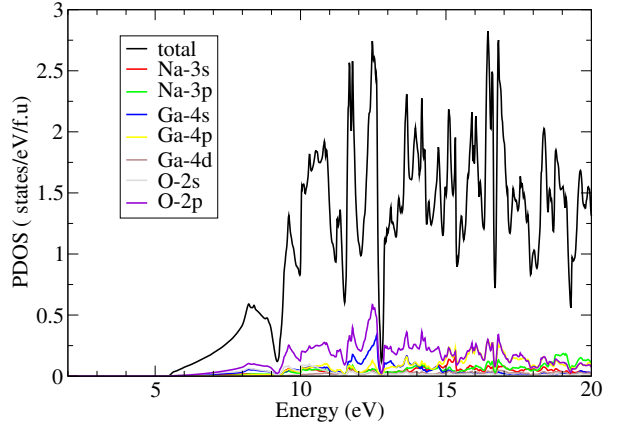
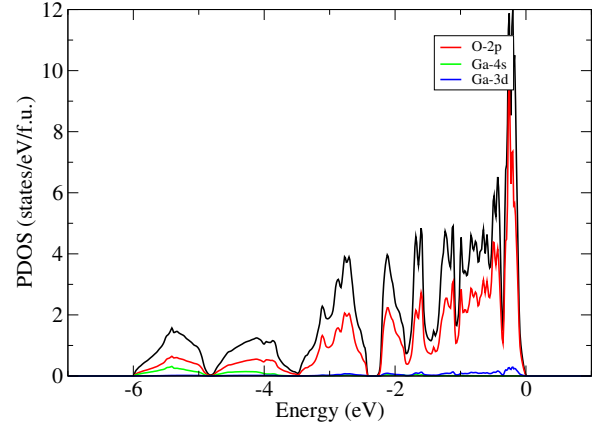
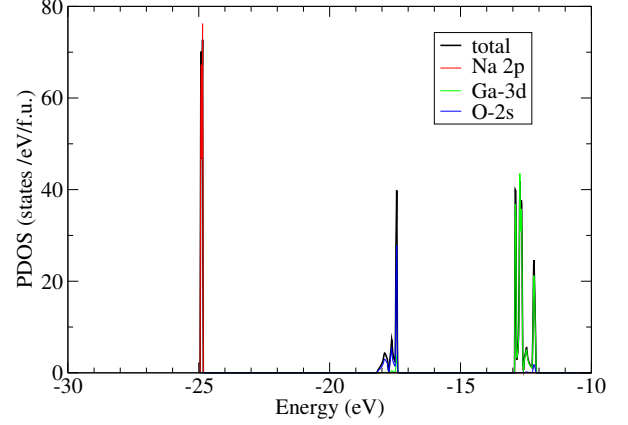


FIG. 15: Total and partial densities of states for (top to bottom) semicore, valence band and conduction band region in NaGaO₂ in *Pna*₂₁ structure.

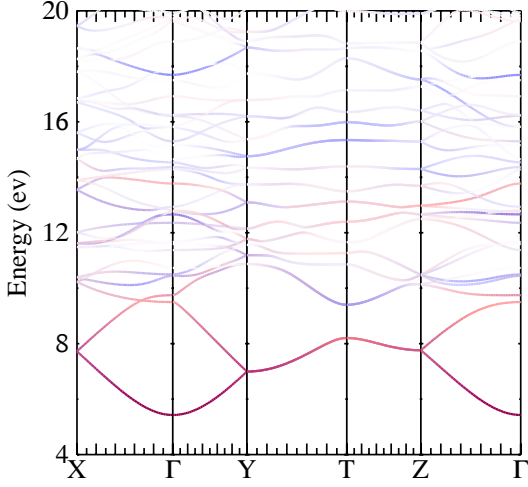


FIG. 16: Conduction band structure of NaGaO₂ in $Pna2_1$ structure and 0.8Σ approximation, showing Ga- s and Na- s contributions in red and blue respectively.

TABLE XIII: Effective masses (in units of the free electron mass) and energy levels in NaGaO₂ in $Pna2_1$ structure.

band	irrep	E (eV)	m_x	m_y	m_z
CBM	Γ_1	5.486	0.33	0.35	0.35
VBM1	Γ_1	0	6.8	2.7	0.5
VBM2	Γ_4	-0.026	0.5	2.7	9.5
VBM3	Γ_2	-0.185	3.4	0.6	3.1

ization onsets of absorption are close to each other while the y onset is larger. In contrast in LiGaO₂ the x and y onsets are close but both larger than the z onset. Thus for light incident on the basal plane (the c -plane) there will be a larger anisotropy in the plane between the two polarizations x and y for NaGaO₂ than for LiGaO₂. On the other hand, in terms of transparent conductor applications, we again see a large splitting between the lowest and next higher conduction band of 4.07 eV, even larger than in LiGaO₂.

The dielectric constant ϵ^∞ (diagonal) tensor components and directional average are given in Table XIV in different approximations. The trends are similar to the LiGaO₂ case. This suggests that the QSGW calculation including the $d\Sigma/dk$ contribution to the matrix elements is an overestimate, perhaps because of neglecting local field effects. The renormalization of the matrix elements gives values close to the GGA and is likely a more realistic estimate.

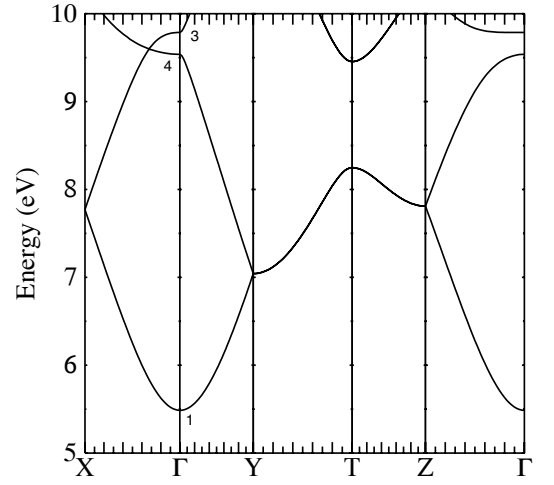
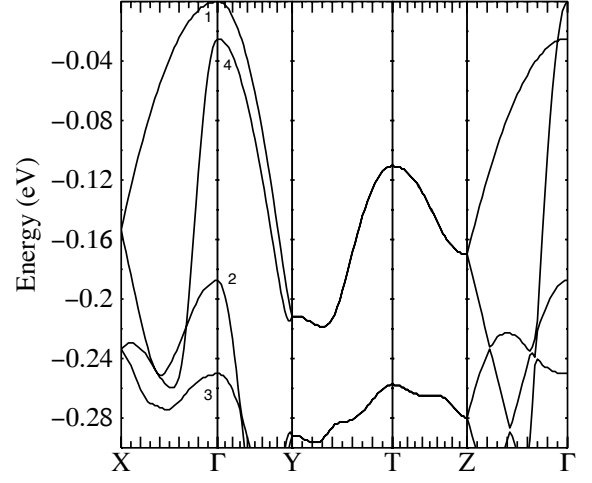


FIG. 17: Symmetry labeled bands for NaGaO₂ in $Pna2_1$ structure. Please note different scales in (top) near valence band maximum and (bottom) conduction band region.

TABLE XIV: Dielectric constants ϵ^∞ of NaGaO₂ in various approximations.

method	ϵ_x^∞	ϵ_y^∞	ϵ_z^∞	$(\epsilon_x^\infty \epsilon_y^\infty \epsilon_z^\infty)^{1/3}$
GGA	2.616	2.606	2.587	2.603
0.8Σ $d\Sigma/dk$	4.268	4.130	4.286	4.227
0.8Σ $d\Sigma/dk = 0$	1.655	1.644	1.648	1.649
0.8Σ rescaling	2.156	2.138	2.137	2.144

F. Band structure of NaGaO₂ in $R\bar{3}m$ and $P4/mmm$ structures.

The band structure of NaGaO₂ in the $R\bar{3}m$ structure is shown in Fig. 20. The band gap is again indirect but with the VBM now between Γ and L and equal to 5.51 eV while the direct gap at Γ is 5.39 eV. On the other hand, in the $P4/mmm$ structure the gap is much smaller. In fact,

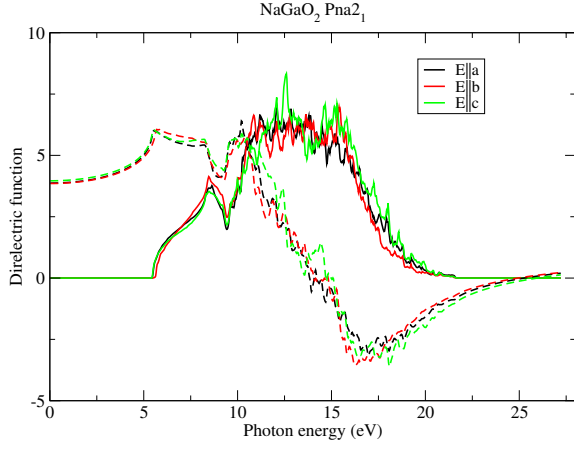


FIG. 18: Imaginary ε_2 and real ε_1 parts of the optical dielectric function for x, y, z directions for NaGaO_2 in $Pna2_1$ structure.

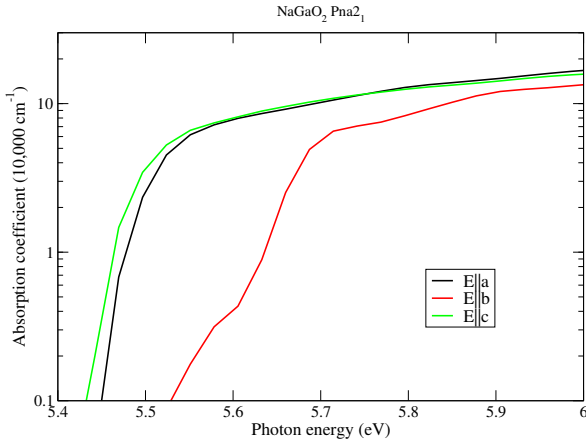


FIG. 19: Absorption coefficient of NaGaO_2 in $Pna2_1$ structure.

in GGA, there is a band overlap and in the 0.8Σ QSGW approximation, the gap is only 0.965 eV. Interestingly, in this case the Ga-3d and O-2s band hybridize.

IV. CONCLUSIONS

In this paper we studied the band structures of LiGaO_2 and NaGaO_2 in three different crystal structures, the ambient pressure equilibrium tetrahedrally bonded $Pna2_1$ and the high-pressure octahedral $R\bar{3}m$ and hypothetical $P4/mmm$ rocksalt type phase, all using the QSGW method. The $Pna2_1$ tetrahedrally bonded structure, which is a cation ordered supercell of the parent wurtzite

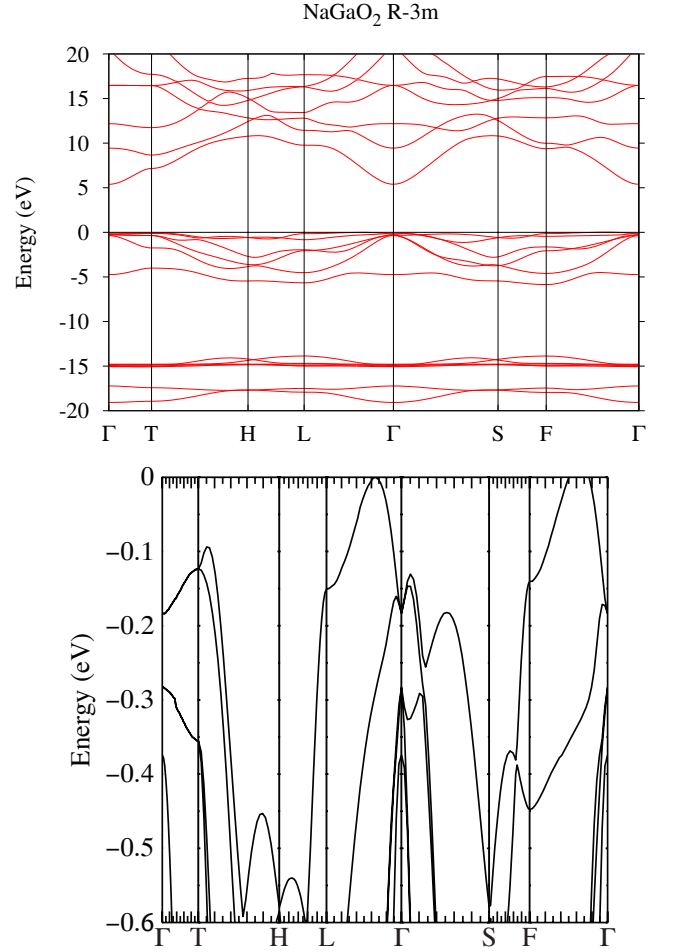


FIG. 20: Band structure of NaGaO_2 in the $R\bar{3}m$ phase in 0.8Σ approximation. The bottom panel shows a zoom in on the VBM region.

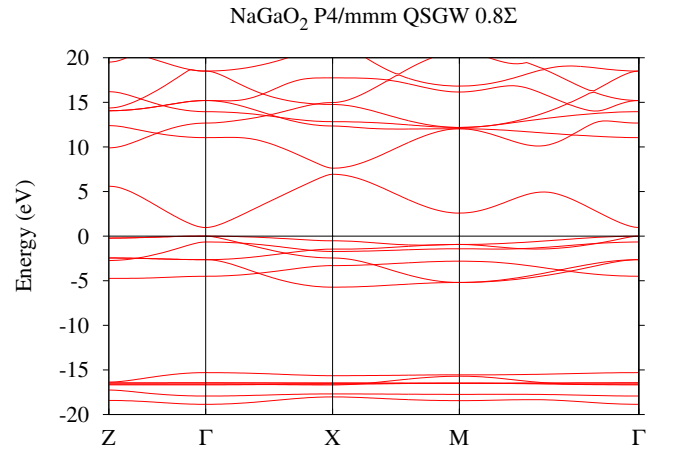


FIG. 21: Band structure of NaGaO_2 in the $P4/mmm$ phase in 0.8Σ approximation.

structure is found in both cases to have lower energy than the octahedrally coordinated $R\bar{3}m$ structure, which is found to be a high-pressure phase with about 20 % smaller volume per formula unit. The materials are ultra-wide band gap semiconductors with gaps of 5.8 eV (LiGaO₂) and 5.5 eV (NaGaO₂) in the $Pna2_1$ structure, not including zero-point motion corrections, which are estimated to be of order -0.2 eV. The gap in the high-pressure phase are of similar magnitude but slightly indirect. The valence band is split in three levels due to the orthorhombic crystal field splitting and lead to anisotropy of the optical absorption onset. Effective mass tensors of the top three valence bands and the conduction band were calculated. In view of previous work, indicating that LiGaO₂ can be n-type doped by Si or Ge, we consider both materials to be promising as ultrawide gap semiconductors for transparent conductor and high-power transistors. In particular, the conduction band symmetry labeling indicates that no optical transitions can occur between the bottom of the conduction band (when n-type doped) to higher conduction bands for energies less than ~ 4.0 eV. As part of this study, we also determined the transition pressures from the tetrahedrally coordinated $Pna2_1$ to the octahedrally coordinated $R\bar{3}m$ phase and a rocksalt type $P4/mmm$ phase and found these to agree well with experiments for LiGaO₂.

- [1] S. Nanamatsu, K. Doi, and M. Takahashi, *Japanese Journal of Applied Physics* **11**, 816 (1972).
- [2] S. N. Gupta, J. F. Vetelino, V. B. Jipson, and J. C. Field, *Journal of Applied Physics* **47**, 858 (1976).
- [3] A. Boonchun and W. R. L. Lambrecht, *Phys. Rev. B* **81**, 235214 (2010).
- [4] P. Knoll and H. Kuzmany, *Phys. Rev. B* **29**, 2221 (1984).
- [5] S. N. Rashkeev, S. Limpijumng, and W. R. L. Lambrecht, *J. Opt. Soc. Am. B* **16**, 2217 (1999).
- [6] M. Marezio, *Acta Crystallographica* **18**, 481 (1965).
- [7] T. Ishii, Y. Tazoh, and S. Miyazawa, *J. Crystal Growth* **186**, 409 (1998).
- [8] W. A. Doolittle, T. Kropewnicki, C. Carter-Coman, S. Stock, P. Kohl, N. M. Jokerst, R. A. Metzger, S. Kang, K. K. Lee, G. May, and A. S. Brown, *Journal of Vacuum Science & Technology B: Microelectronics and Nanometer Structures Processing, Measurement, and Phenomena* **16**, 1300 (1998).
- [9] A. Christensen, W. A. Doolittle, and S. Graham, *IEEE Transactions on Electron Devices* **52**, 1683 (2005).
- [10] K. Sakurada, A. Kobayashi, Y. Kawaguchi, J. Ohta, and H. Fujioka, *Applied Physics Letters* **90**, 211913 (2007), <https://doi.org/10.1063/1.2737928>.
- [11] T. Omata, K. Tanaka, A. Tazuke, K. Nose, and S. Otsuka-Yao-Matsuo, *J. Appl. Phys.* **103**, 083706 (2008).
- [12] T. Omata, M. Kita, K. Nose, K. Tachibana, and S. Otsuka-Yao-Matsuo, *Jpn. J. Appl. Phys.* **50**, 031102 (2011).
- [13] I. Ohkubo, C. Hirose, K. Tamura, J. Nishii, H. Saito, H. Koinuma, P. Ahemt, T. Chikyow, T. Ishii, S. Miyazawa, Y. Segawa, T. Fukumura, and M. Kawasaki, *Journal of Applied Physics* **92**, 5587 (2002).
- [14] A. Boonchun and W. R. L. Lambrecht, in *Oxide-based Materials and Devices II*, Proceedings of SPIE, Vol. 7940, edited by F. H. Terani, D. C. Look, and D. J. Rogers, International Society for Optics and Photonics (SPIE, 2011) pp. 129–134.
- [15] A. Boonchun, K. Dabsamut, and W. R. L. Lambrecht, *Journal of Applied Physics* **126**, 155703 (2019).
- [16] K. Dabsamut, A. Boonchun, and W. R. L. Lambrecht, *Journal of Physics D: Applied Physics* (2020).
- [17] C. A. Lenyk, M. S. Holston, B. E. Kananen, L. E. Halliburton, and N. C. Giles, *Journal of Applied Physics* **124**, 135702 (2018).
- [18] D. Skachkov, W. R. L. Lambrecht, K. Dabsamut, and A. Boonchun, *Journal of Physics D: Applied Physics* **53**, 17LT01 (2020).
- [19] K. Sasaki, M. Higashiwaki, A. Kuramata, T. Masui, and S. Yamakoshi, *J. Cryst. Growth* **378**, 591 (2013), the 17th International Conference on Molecular Beam Epitaxy.
- [20] A. J. Green, K. D. Chabak, E. R. Heller, R. C. Fitch, M. Baldini, A. Fiedler, K. Irmscher, G. Wagner, Z. Galazka, S. E. Tetlak, A. Crespo, K. Leedy, and G. H. Jessen, *IEEE Electron Device Letters* **37**, 902 (2016).
- [21] J. T. Wolan and G. B. Hoflund, *J. Vac. Sci. Tech. A* **16**, 3414 (1998).
- [22] C. Chen, C.-A. Li, S.-H. Yu, and M. M. Chou, *Journal of Crystal Growth* **402**, 325 (2014).
- [23] N. W. Johnson, J. A. McLeod, and A. Moewes, *Journal of Physics: Condensed Matter* **23**, 445501 (2011).
- [24] A. Ratnaparkhe and W. R. L. Lambrecht, *Physica Status Solidi (b)* **257**, 1900317 (2020).
- [25] A. Ratnaparkhe and W. R. L. Lambrecht, *Applied Physics Letters* **110**, 132103 (2017).
- [26] MP, <https://materialsproject.org/>.
- [27] J. P. Perdew, K. Burke, and M. Ernzerhof, *Phys. Rev. Lett.* **77**, 3865 (1996).
- [28] <http://www.questaal.org/>.
- [29] D. Pashov, S. Acharya, W. R. Lambrecht, J. Jackson, K. D. Belashchenko, A. Chantis, F. Jamet, and M. van Schilfgaarde, *Computer Physics Communications* , 107065 (2019).
- [30] M. Methfessel, M. van Schilfgaarde, and R. A. Casali, in *Electronic Structure and Physical Properties of Solids. The Use of the LMTO Method*, Lecture Notes in Physics, Vol. 535, edited by H. Dreyssé (Berlin Springer Verlag, 2000) p. 114.
- [31] T. Kotani and M. van Schilfgaarde, *Phys. Rev. B* **81**, 125117 (2010).
- [32] P. Giannozzi, S. Baroni, N. Bonini, M. Calandra, R. Car, C. Cavazzoni, D. Ceresoli, G. L. Chiarotti, M. Cococcioni, I. Dabo, A. D. Corso, S. de Gironcoli, S. Fabris, G. Fratesi, R. Gebauer, U. Gerstmann, C. Gougoussis, A. Kokalj, M. Lazzeri, L. Martin-Samos, N. Marzari, F. Mauri, R. Mazzarello, S. Paolini, A. Pasquarello, L. Paulatto, C. Sbraccia, S. Scandolo, G. Sclauzero, A. P. Seitsonen, A. Smogunov, P. Umari, and R. M. Wentzcovitch, *Journal of Physics: Condensed Matter* **21**, 395502 (2009).
- [33] L. Hedin, *Phys. Rev.* **139**, A796 (1965).
- [34] L. Hedin and S. Lundqvist, in *Solid State Physics, Advanced in Research and Applications*, Vol. 23, edited by F. Seitz, D. Turnbull, and H. Ehrenreich (Academic Press, New York, 1969) pp. 1–181.
- [35] T. Kotani, M. van Schilfgaarde, and S. V. Faleev, *Phys. Rev. B* **76**, 165106 (2007).
- [36] M. van Schilfgaarde, T. Kotani, and S. V. Faleev, *Phys. Rev. B* **74**, 245125 (2006).
- [37] C. Bhandari, M. van Schilfgaarde, T. Kotani, and W. R. L. Lambrecht, *Phys. Rev. Materials* **2**, 013807 (2018).
- [38] A. N. Chantis, M. van Schilfgaarde, and T. Kotani, *Phys. Rev. Lett.* **96**, 086405 (2006).
- [39] D. Deguchi, K. Sato, H. Kino, and T. Kotani, *Japanese Journal of Applied Physics* **55**, 051201 (2016).
- [40] B. Cunningham, M. Grüning, P. Azarhoosh, D. Pashov, and M. van Schilfgaarde, *Phys. Rev. Materials* **2**, 034603 (2018).
- [41] M. Marezio and J. Remeika, *Journal of Physics and Chemistry of Solids* **26**, 1277 (1965).
- [42] L. Lei, T. Irifune, T. Shinmei, H. Ohfuji, and L. Fang, *Journal of Applied Physics* **108**, 083531 (2010).
- [43] L. Lei, H. Ohfuji, J. Qin, X. Zhang, F. Wang, and T. Irifune, *Solid State Communications* **164**, 6 (2013).
- [44] G. F. Koster, J. O. Dimmock, R. G. Wheeler, and H. Statz, *Properties of the Thirty-Two Point Groups* (MIT Press, Cambridge, MA, 1963).
- [45] W. R. L. Lambrecht, A. V. Rodina, S. Limpijumng, B. Segall, and B. K. Meyer, *Phys. Rev. B* **65**, 075207

- (2002).
- [46] S. Tunnas, P. Mackonis, R. Nedzinskas, L. Trinkler, B. Berzina, V. Korsaks, L. Chang, and M. Chou, *Applied Surface Science* **421**, 837 (2017).
- [47] Z. H. Levine and D. C. Allan, *Phys. Rev. Lett.* **63**, 1719 (1989).
- [48] W. R. L. Lambrecht, C. Bhandari, and M. van Schilf-gaarde, *Phys. Rev. Materials* **1**, 043802 (2017).
- [49] J. P. Nery and P. B. Allen, *Phys. Rev. B* **94**, 115135 (2016).
- [50] A. Miglio, V. Brousseau-Couture, E. Godbout, G. Antonius, Y.-H. Chan, S. G. Louie, M. Côté, M. Giantomassi, and X. Gonze, *npj Computational Materials* **6** (2020), 10.1038/s41524-020-00434-z.
- [51] C. Verdi and F. Giustino, *Phys. Rev. Lett.* **115**, 176401 (2015).
- [52] Y. Hinuma, G. Pizzi, Y. Kumagai, F. Oba, and I. Tanaka, *Computational Materials Science* **128**, 140 (2017).
- [53] S. Weise and H. Neumann, *Crystal Research and Technology* **31**, 659 (1996), <https://onlinelibrary.wiley.com/doi/pdf/10.1002/crat.2170310523>.